Optical Tactile Force Sensing with a Soft Transparent Sensory Skin Using Laser Time-of-Flight Measurement and Nonlinear Modeling

Aleš Zore, Marina Babić, Marko Munih, *Member, IEEE*, and Roman Kamnik, *Member, IEEE*

***Abstract*— This work presents a machine-learning-based framework for predicting applied contact force from the optical response of a time-of-flight (ToF) sensor embedded in a soft, optically transparent tactile sensing medium, SoftSkin. The SoftSkin medium acts as a light-guiding structure, enabling light propagation via total internal reflection. External pressure deforms the light-guide material, resulting in measurable changes in the optical response. A robotic test setup equipped with a force–torque sensor enabled controlled and repeatable experiments. Training datasets were collected at three indentation velocities and six applied force levels. Three multilayer perceptron (MLP) architectures were developed and evaluated. The single-input method used only photon counts, whereas the dual-input method incorporated temporal ambient-light conditions. A third approach, the derivative-enhanced dual-input method, additionally integrates temporal gradients of the photon response. For each MLP model, a Random Forest (RF) residual corrector was applied to reduce prediction errors. Performance was evaluated on an independent test set comprising unseen force magnitudes at three indentation velocities. All MLP–RF models achieved a mean absolute prediction error below 1 N, with the derivative-enhanced dual-input model demonstrating the best performance. The results confirm that ToF-based optical tactile sensing, combined with lightweight neural network architectures and residual learning, enables accurate reconstruction of dynamic force profiles despite sensor noise and the limited frame rate of the ToF sensor.**

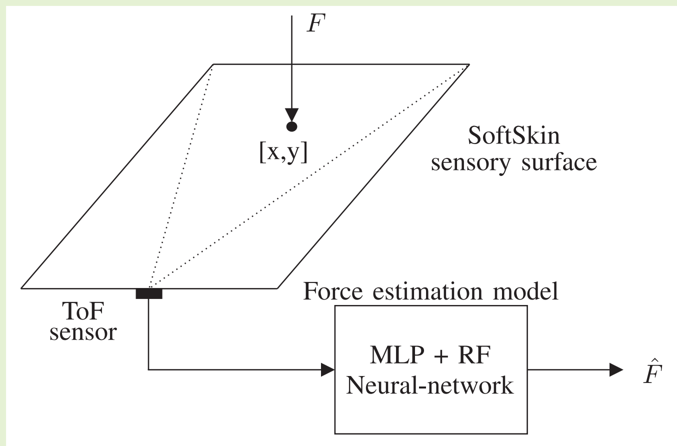

***Index Terms*— applied contact force prediction, LIDAR, light-guide, neural network (NN), soft sensor skin, tactile sensing, time-of-flight (ToF)**

I. Introduction

The capability to sense physical interactions across a surface opens new possibilities in robotics. Interaction with the environment is essential not only in social robotics but also increasingly in industrial applications, particularly in collaborative robotics. It is no longer sufficient to detect whether contact has occurred; it is also necessary to determine the location of contact, the magnitude of the applied force, and the contact area of the current interaction.

This work was funded by the European Commission's HORIZON EUROPE Research and Innovation Actions under GA number 101070310 and by Slovenian Research Agency (funding No. P2-0228).

All authors contributed equally to the work presented in this paper.

A. Zore, M. Babić, M. Munih and R. Kamnik are with University of Ljubljana, Faculty of Electrical Engineering, Tržaška cesta 25, 1000 Ljubljana, Slovenia (e-mail: ales.zore@fe.uni-lj.si)

Over the past decades, numerous tactile pressure-sensing technologies have been developed, with the most established operating principles being piezoresistive, capacitive, piezoelectric, and triboelectric. Piezoresistive sensors, including strain gauges, operate by measuring changes in resistance under mechanical deformation and are valued for their sensitivity, stability, low noise, and reliability [1]. Capacitive sensors measure variations in capacitance caused by changes in electrode spacing, enabling high sensitivity at low power consumption [2]. Piezoelectric sensors directly convert mechanical stress into voltage and exhibit excellent dynamic response [1], [2]. Triboelectric sensors exploit contact electrification and electrostatic induction to generate an electrical output, enabling self-powered operation and high sensitivity for flexible, large-area applications [2], [3]. Inductive pressure sensors, a broader class of magnetic sensors, measure the diaphragminduced displacement of a ferromagnetic core, which alters the voltage ratio between two windings in proportion to the applied pressure. This design provides high sensitivity, mechanical robustness, and negligible hysteresis [4].

Optical pressure sensors represent another important class, exploiting pressure-induced changes in the properties of light, such as intensity, phase, wavelength, or polarisation. They offer high sensitivity, immunity to electromagnetic interference, and remote sensing capability [5].

Despite these advantages, each technology faces specific limitations: a) capacitive and piezoresistive designs are prone to hysteresis, b) piezoresistive and piezoelectric sensors exhibit temperature dependence and drift, c) piezoelectric sensors cannot measure static forces, and d) triboelectric, capacitive and optical sensors remain susceptible to environmental disturbances.

There are various existing optical tactile sensing technologies, including camera-based visuotactile systems, FTIR, lightguides with embedded LEDs and photodetectors, fibre-optic Bragg gratings (FBG), and other specialised optical modalities. Camera-based visuotactile sensors have the highest spatial resolution, 640×480 pixels over $20 \times 20\ \mathrm{mm}^2$, with sensing range up to $15\ \mathrm{N}$ [6]. Its mechanical design is best suited to a fingertip design but struggles at large scales due to high cost and difficulty achieving large-area coverage. FBG implementation shows good repeatability and flexibility with a sensing range up to $10\ \mathrm{N}$ [7]. It offers high scalability but at a high cost and temperature compensation.

A promising optical approach for precise touch and pressure detection based on light behaviour is frustrated total internal reflection (FTIR). This method relies on total internal reflection (TIR) of infrared light within an optically transparent medium until contact with an external object locally disrupts the reflection [8]–[11]. High sensitivity, good scalability across surfaces ranging from relatively small to larger ones (up to A4 paper size), and the capability for simultaneous multi-touch detection make FTIR-based solutions well-suited for robotic applications.

Recently, Bacher et al. [12] implemented direct time-of-flight (ToF) LiDAR-based sensing as an evolution of FTIR sensing technology. The combination of FTIR and ToF enables faster response times, increased flexibility at lower integration cost, and adaptability to large or non-planar sensing surfaces. Furthermore, the FTIR optical principle allows sensorisation of extended areas without requiring individual wiring for each taxel.

The soft, transparent sensory skin (SoftSkin) incorporates a ToF sensor and exploits TIR within an optically transparent medium. Because the sensory surface is compliant, it deforms upon contact and redirects the injected light toward the ToF sensor. The reflected optical response, particularly its intensity, depends on multiple factors, including the optical properties of the medium (transmittance, reflectance, scattering, and refractive index), the distance between the contact point and the ToF sensor, ambient lighting conditions, the curvature of the sensory surface, and the magnitude of the applied force. However, the mapping between ToF sensor responses and environmental and interaction parameters is highly nonlinear and coupled.

Neural networks (NNs) are computational models inspired by biological nervous systems that can approximate complex, highly nonlinear relationships between inputs and outputs through data-driven learning. Neural networks consist of interconnected processing units (neurons) that map inputs to outputs through weighted connections and activation functions. Among the most widely used architectures are multilayer perceptrons (MLPs), which serve as universal function approximators capable of representing arbitrary nonlinear mappings [13]. Key advantages of NNs include their ability to learn input–output relationships directly from data, robustness to noise, and effectiveness in handling nonlinear and high-dimensional problems.

In practical applications, NNs have been successfully used for force prediction. For example, Radhakrishnan and Nandan [14] employed NNs to estimate milling forces from cutting parameters, achieving higher accuracy than traditional regression approaches. Similarly, NN models have been applied to the prediction of pulling force, demonstrating their ability to capture complex input–output relationships that are difficult to model analytically [15]. Nonlinear modelling has also been used to estimate the position and distribution of contact forces in a vision-based fingertip sensor [16]. Furthermore, Min et al. [17] applied deep NNs to decode normal and shear forces in real time.

This work presents a machine-learning-based framework for predicting the tactile force applied to the surface of the SoftSkin optical tactile sensor. Three MLP architectures were developed to model the nonlinear dependence of the sensor response on the applied force. These models were further combined with a Random Forest (RF) residual corrector to improve prediction accuracy. The proposed approach was validated using datasets acquired with a robotic setup during controlled indentation tasks and evaluated through line-plot analysis and quantitative performance metrics, with particular emphasis on the mean absolute error (MAE). NN training was conducted at six discrete force levels and three indentation velocities, whereas validation employed randomly selected force levels up to 60 N.

II. SoftSkin - soft sensory surface

SoftSkin is a sensory surface composed of an elastic silicone rubber material, Crystalflex, with mechanical properties comparable to human skin. Owing to its elasticity and optical transparency, the material can serve as a light-guiding medium, enabling light propagation via TIR. The sensory surface can integrate multiple ToF sensors and can be mounted on both flat and curved substrates. Figure 1 illustrates the SoftSkin sensory surface with four embedded ToF sensors.

The Crystalflex material has a Shore A hardness of 20, corresponding to a soft elastomeric range on the Shore hardness scale [18]. The most relevant optical parameters governing light propagation within the light-guiding material are the transmittance $T = 88.2\ \%$, diffuse reflectance $R_d = 1.9\ \%$, scattering coefficient $\mu_s = 0.1\ \mathrm{cm}^{-1}$ and refractive index $n = 1.398$, measured over a spectral range from $175\ \mathrm{nm}$ to $3300\ \mathrm{nm}$ [19].

This article has been accepted for publication in IEEE Sensors Journal. This is the author's version which has not been fully edited and
content may change prior to final publication. Citation information: DOI 10.1109/JSEN.2026.3713612

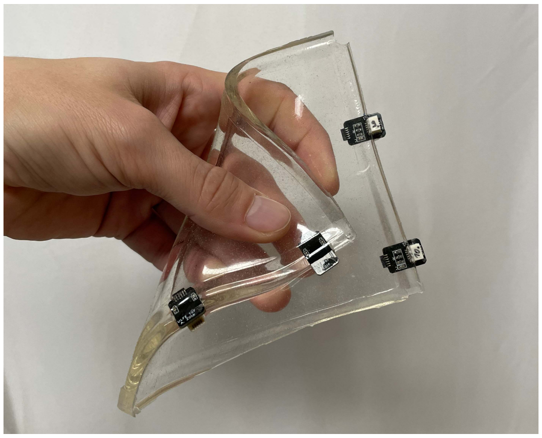

Fig. 1: SoftSkin sensor surface made of transparent elastic silicone rubber with four embedded ToF sensors.

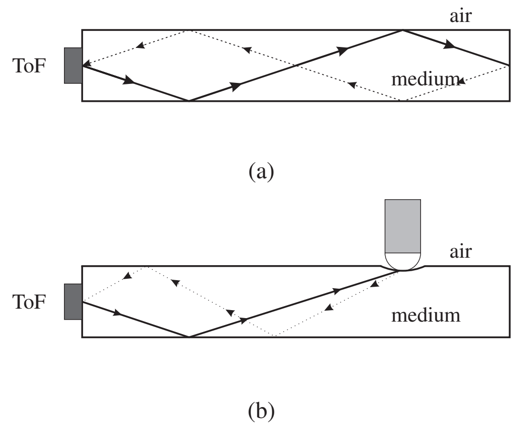

Fig. 2: SoftSkin touch detection working principle: (a) total internal reflection - TIR within the light-guide medium, and (b) deformation of the light-guide material in mechanically compliant medium. The solid line represents the emitted light, whereas the dotted line denotes the reflected light.

A ToF sensor is integrated at the edge of the light-guide material and emits infrared (IR) light into the medium, where it propagates via TIR phenomena. Under ideal conditions, the light reaches the distal end of the light-guide and is refracted back, ultimately returning to the ToF sensor [12] (see Figure 2a). The measured time-of-flight of the reflected signal is related to the effective optical path length of the light guide. The reflected signal acquired in the absence of external contact is referred to as the baseline.

Based on the physical properties of the light-guide material, two touch-sensing principles can be distinguished. In SoftSkin, light emitted by the ToF sensor propagates through the light guide via TIR, since $n_{\mathrm{OptoSkin}} > n_{\mathrm{air}}$ (Figure 2a). Upon contact with OptoSkin, light propagation is locally disturbed within the contact region due to interaction with the environment ($n_{\mathrm{environment}} \neq n_{\mathrm{air}}$). This disturbance arises from two mechanisms: scattering induced by FTIR when $n_{\mathrm{environment}} \approx n_{\mathrm{OptoSkin}}$, and deformation of the elastic material (Figure 2b). In the latter case, the TIR condition, which is governed by Snell's law and the Fresnel equations, is satisfied only when the angle of incidence exceeds the critical angle [20]. The optical response caused by surface deformation is significantly stronger than that produced by FTIR. During deformation, light is redirected toward the ToF sensor with increased intensity, whereas in FTIR, it primarily scatters at the contact region rather than directly reflects.

The considered SoftSkin prototype has dimensions of $210\ \mathrm{mm} \times 300\ \mathrm{mm}$ and a thickness of $5\ \mathrm{mm}$. Four ToF sensors are embedded along the two shorter sides, arranged as two opposing sensor pairs, as illustrated in Figure 3. Although the prototype incorporates multiple ToF sensors, the present analysis considers only the response of a single sensor. The selected ToF sensor is highlighted in red. The expansion to multiple sensors primarily increases the sensing area. The sensitivities of different ToF sensors should not differ significantly, so generalisation based on measurements from one sensor is meaningful and justified.

AMS Osram TMF8828 ToF sensors were used in this study. The TMF8828 is a compact modular device that integrates a vertical-cavity surface-emitting laser (VCSEL) and an array of

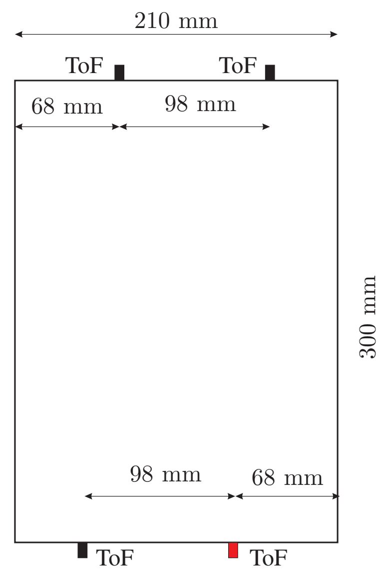

Fig. 3: SoftSkin prototype: physical dimensions and placement of ToF sensors.

64 (8×8) single-photon avalanche diodes (SPADs). A multi-lens array provides a wide field of illumination (FoI) and field of view (FoV) of $41^\circ \times 52^\circ$. One of the most advantageous features of the sensor is its ability to provide a temporal profile in histogram form for each SPAD. Such profile data enables the application of advanced custom algorithms for force estimation.

Nominally, each SPAD histogram response contains 128 bins representing discrete and uniformly spaced distance intervals within a measurement range of up to $1\ \mathrm{m}$, resulting in $8 \cdot 8 \cdot 128 = 8192$ values. The first 15 bins are reserved for crosstalk calibration, and because the prototype length is $30\ \mathrm{cm}$, the effective response is limited to 37 usable radial bins. Additionally, sensor operation was accelerated by employing the 4×4 mode, yielding $4 \cdot 4 \cdot 37 = 592$ values per ToF sensor response. Because the sensor surface is

This article has been accepted for publication in IEEE Sensors Journal. This is the author's version which has not been fully edited and content may change prior to final publication. Citation information: DOI 10.1109/JSEN.2026.3713612

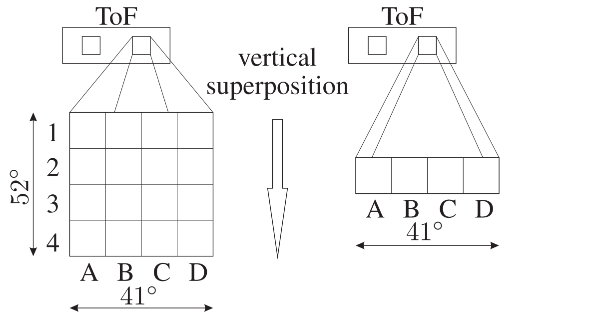

Fig. 4: Arrangement of SPADs in 4×4 mode for 3D spatial sensing and after vertical superposition for 2D planar sensing (ToF sensor embedded in the medium). Layers are numbered 1–4, and beams are denoted A–D.

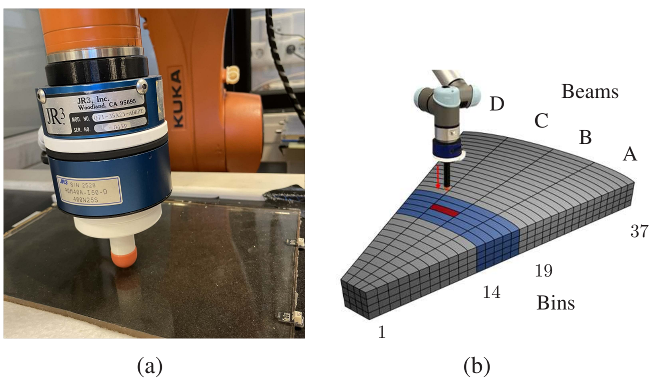

Fig. 5: Application of pressure using a robot: (a) touch position at a fixed location at a distance of $d = 150$ mm, and (b) corresponding touch position in the ToF sensor histogram response map.

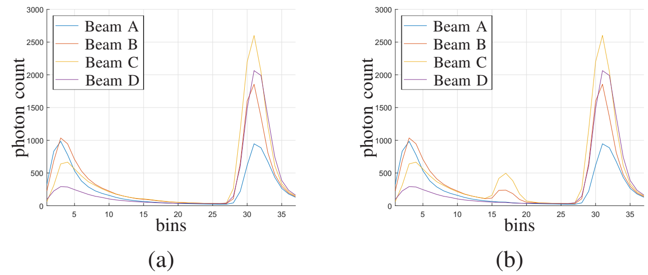

Fig. 6: Histogram responses: (a) baseline with no external contact, and (b) applied touch at 150 mm from ToF sensor.

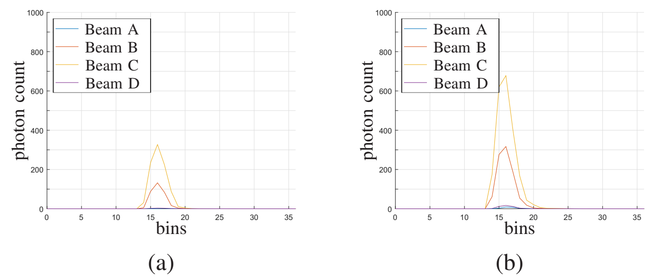

Fig. 7: Histogram responses under different applied forces at the distance of 150 mm from ToF sensor with subtracted baseline: (a) $F = 20$ N, and (b) $F = 50$ N.

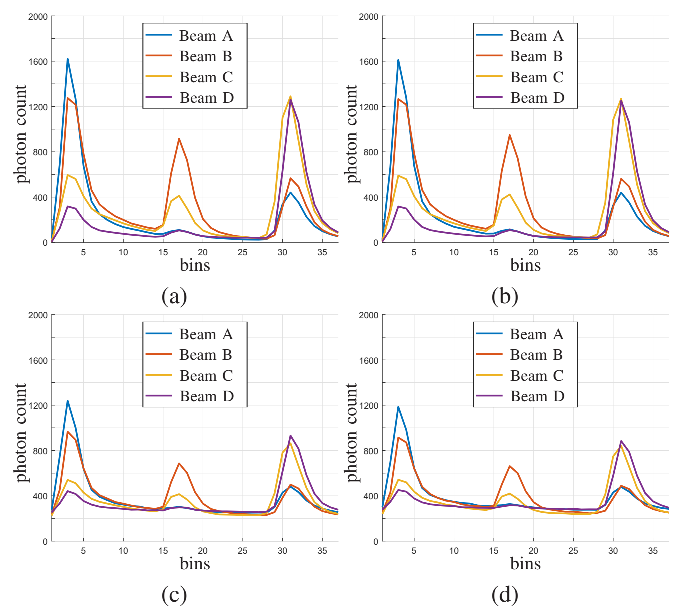

Fig. 8: Histogram responses in different ambient light conditions with applied pressure of $F = 30$ N: (a) indoor dark conditions $E = 0.84$ lx, (b) indoor lights on $E = 1205$ lx, (c) outdoor sunlight in shadow $E = 3320$ lx, and (d) outdoor direct sunlight $E = 4500$ lx.

effectively two-dimensional, the four layers used in 3D sensing are combined into a single layer, resulting in four beams corresponding to discrete angular values (denoted A–D). An illustration of the configuration and notation of the sensory elements is provided in Figure 4 and Figure 5b.

Histogram responses of the four beams, obtained by combining the four layers, are shown in Figure 6. Figure 6a presents the ToF response of SoftSkin under the no-touch condition, which defines the baseline pattern. The baseline response is consistent with respect to material and geometric properties but may vary with ambient light conditions.

Two peaks can be observed, corresponding to crosstalk and to the beginning and end of the light-guide medium, consistent with the explanation in Figure 2a. The graph in Figure 6b presents the response obtained under applied tactile pressure at a distance of $d = 150$ mm from the ToF sensor. Upon contact (see Figure 5), the SoftSkin surface deforms, and light is reflected from the contact region, as illustrated in Figure 2b, resulting in an additional peak between bins 15 and 20.

In principle, ToF sensors measure the time-of-flight of IR light reflected from the deformed surface at the contact region. Because the deformation depends on the applied contact force, the ToF sensor response (photon count) is related to the applied force. Figure 7 illustrates histogram responses for two different applied forces with baseline subtraction. Figure 7a shows the response at 20 N, and Figure 7b shows the response at 50 N, both at a distance of 150 mm. A higher applied force clearly results in a higher photon-count response; however, the relationship is nonlinear and involves multiple beam signals.

The ToF sensor used is not resistant to ambient light.

Figure 8 shows histogram responses at four different ambient light conditions (illumination E) with applied pressure with the robot: indoor dark ($E = 0.84$ lx), indoor with lights on ($E = 1025$ lx), outdoor in shadow ($E = 3320$ lx), and outdoor at the direct sunlight ($E = 4500$ lx). Ambient light illumination was measured with a calibrated and accredited LMT B 360 digital illuminance meter (calibration certificate E0375/2024 and accreditation certificate 7604). In histogram responses, a baseline (left and right peak values) and an applied touch of $F = 30$ N (the middle peak) can be visible.

A significant difference is observed between indoor (Figures 8a and 8b) and outdoor ambient light conditions (Figures 8c and 8d). In indoor measurements, outdoor sunlight was completely blocked. Comparing indoor dark and lights on conditions, there is no significant difference despite a significant difference in illumination (0.84 lx vs 1205 lx). Baseline responses (left and right peaks) differ by 0.5 %, and sensed touch responses (the middle peak) differ by 3.5 %. There is an obvious difference in histogram responses in outdoor experiments. A vertical offset is present compared to indoor conditions, and the flattening of the sensor response can also be noticeable.

A higher offset is observed at higher illumination levels, and the response flattens. The cause presumably lies in sunlight, which spans a broad spectrum from infrared to ultraviolet.

A SoftSkin implementation is primarily intended for indoor applications, but with the addition of a special elastic, light-impermeable cover material, the ambient light effect can be mitigated.

III. METHODOLOGY

The analysis of force sensing using a soft, optically transparent sensory surface was conducted in a robotic test cell, shown in Figure 9. The experimental setup consists of a KUKA KR10 robotic arm equipped with two force and torque (F/T) sensors mounted in series on the end effector, together with a custom-designed indenter tool. The first F/T sensor (JR3 Q71-35A25-ADEPT), featuring an analogue output and an adjustable comparator, was used as a force-threshold trigger. The second F/T sensor (JR3 90M40A-I50-D), which provides a digital, continuous output, was employed to measure the contact force applied by the robot.

The indenter design allows interchangeable tool tips with indenters of different shapes and sizes. For all subsequent localisation evaluation experiments, a round indenter with a diameter of 22 mm was used, approximating the dimensions of a human finger. The indenter was entirely fabricated from PLA using 3D printing.

The primary task of the robot is to ensure accurate positioning of the indenter on the SoftSkin surface and to apply the desired contact force through controlled penetration of the SoftSkin material. The comparator output of the analogue F/T sensor is connected to a digital input of the robot controller and is set high when the applied force exceeds a predefined threshold, thereby stopping further penetration. The digital F/T sensor continuously transmits the measured force and torque data to a PC via the UDP protocol at a sampling rate of 100 Hz. The ToF sensor communicates with the SoftSkin acquisition system via the I^2C protocol using a Raspberry Pi 4B, and provides data at the sampling rate of 9 Hz. The acquisition system then transmits data packets via UDP to the data acquisition and processing PC, where online processing is performed within a MATLAB/Simulink model.

To analyse the relationship between photon response and applied force, an indenter was positioned at a single position at a fixed distance of $d = 150$ mm from the ToF sensor, as shown in Figure 5. To capture dynamic variability under different loading conditions, data were collected at three indentation velocities corresponding to linear motion perpendicular to the SoftSkin surface: 0.1 mm/s, 1 mm/s, and 5 mm/s. The training set comprised data acquired at six discrete robot-applied force levels ranging from $10-60$ N in increments of 10 N under varying ambient conditions. For each combination of force and velocity, five repetitions of the applied touch were performed. Force data obtained during training measurements are visualised in Figure 10. The initial gradual increase in force corresponds to the lowest penetration velocity (up to approximately 3200 s), followed by the signal captured at the medium penetration velocity (between 3200 and 3700 s). In contrast, the final segment corresponds to penetration at the highest velocity.

In contrast, the test set comprised independent measurements with force magnitudes not included in the training data (e.g., intermediate values such as 12 N or 33 N). For each penetration velocity, 10 randomly selected force values were recorded, resulting in a total of 30 applied forces in the test set presented in the Results section.

A. Data-set structure

From Figures 6 and 7, it can be observed that the applied force at a position of 150 mm from the ToF sensor is characterised by responses within the bin range from 14 to 19. Histogram values outside this range remain unchanged regardless of the applied force. Consequently, the ToF data-set for a contact position used in this analysis is reduced to 20 values, corresponding to the responses of four beams and five bins, as illustrated by the blue region in Figure 5b. The remaining histogram responses do not contain pressure-related information for this specific touch location. A single ToF response is therefore represented by the array D_{ToF}.

$$D_{\mathrm{ToF}}(i,j) = \begin{bmatrix} D_{Aj} \\ D_{Bj} \\ D_{Cj} \\ D_{Dj} \end{bmatrix} = \begin{bmatrix} D_{A1} & D_{A2} & D_{A3} & D_{A4} & D_{A5} \\ D_{B1} & D_{B2} & D_{B3} & D_{B4} & D_{B5} \\ D_{C1} & D_{C2} & D_{C3} & D_{C4} & D_{C5} \\ D_{D1} & D_{D2} & D_{D3} & D_{D4} & D_{D5} \end{bmatrix} \tag{1}$$

where i denotes the beam index and j denotes the bin index in the corresponding ToF data set. For subsequent use as input to a NN, the individual values of the D_{ToF} data-set were vectorised and normalised.

This article has been accepted for publication in IEEE Sensors Journal. This is the author's version which has not been fully edited and content may change prior to final publication. Citation information: DOI 10.1109/JSEN.2026.3713612

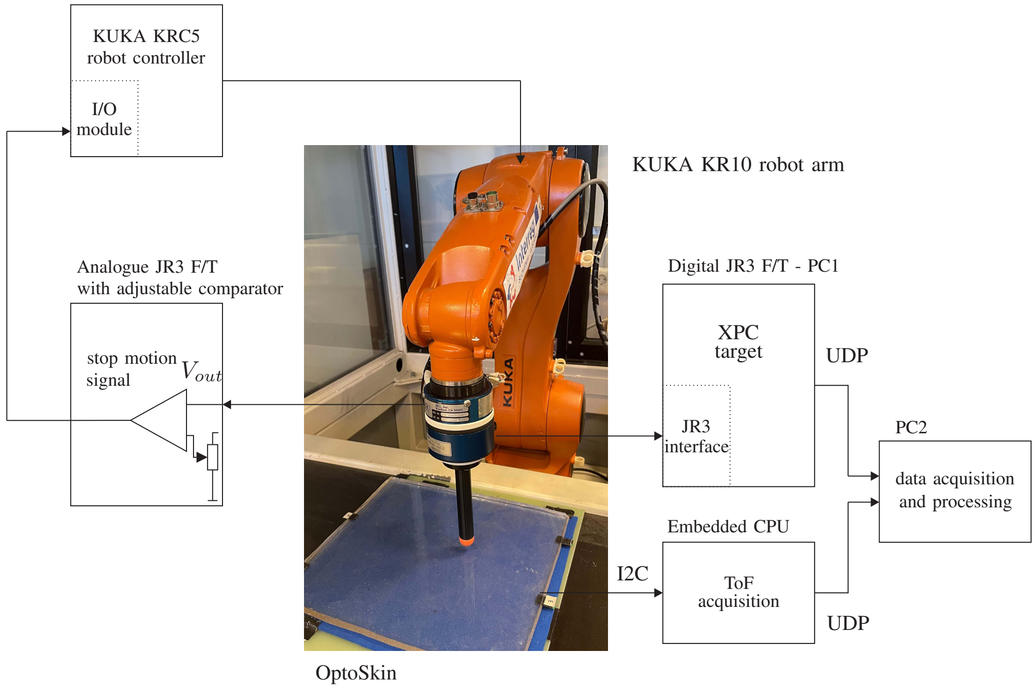

Fig. 9: Robot test setup for OptoSkin characterisation. The KUKA KR10 robotic manipulator is used for indenter positioning and controlled force application on the OptoSkin surface. Two force/torque sensors, providing analogue and digital outputs, are employed for contact force measurement.

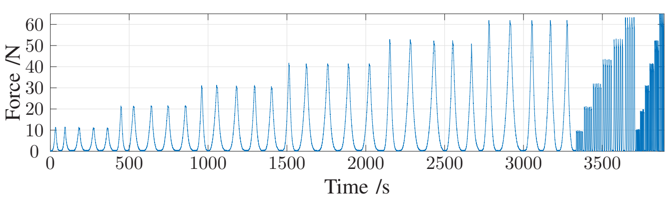

Fig. 10: Force data for training data-set at six discrete applied force levels at three indentation velocities.

A single ToF response, converted into vector form d_{ToF} and representing one NN input, is defined as

$$d_{ToF} = \begin{bmatrix} D_{A1} & D_{A2} & \cdots & D_{D4} & D_{D5} \end{bmatrix}'. \tag{2}$$

During the normalisation process, each element of d_{ToF} is linearly scaled to the interval $[0, 1]$. The data are normalised using the global minimum and maximum ToF sensor responses across the entire measurement data-set. The resulting normalised ToF data set is denoted by $\overline{d}_{\mathrm{ToF}}$.

The complete data-set for time samples $t = 1, \ldots, n$, consisting of vectorised single ToF responses $\overline{d}_{\mathrm{ToF}}$ forms the training input matrix $X_{\mathrm{ToF}} \in \mathbb{R}^{20\times n}$ for use as input to the NN.

$$\begin{aligned} X_{\mathrm{ToF}} &= \begin{bmatrix} \overline{d}_{\mathrm{ToF},1} & \overline{d}_{\mathrm{ToF},2} & \ldots & \overline{d}_{\mathrm{ToF},n} \end{bmatrix} \\ &= \begin{bmatrix} \overline{D}_{A1,1} & \overline{D}_{A1,2} & \ldots & \overline{D}_{A1,n} \\ \overline{D}_{A2,1} & \overline{D}_{A2,2} & \ldots & \overline{D}_{A2,n} \\ \vdots & \vdots & \ddots & \vdots \\ \overline{D}_{D4,n} & \overline{D}_{D4,2} & \ldots & \overline{D}_{D4,n} \\ \overline{D}_{D5,n} & \overline{D}_{D5,2} & \ldots & \overline{D}_{D5,n} \end{bmatrix} \end{aligned} \tag{3}$$

Similarly, the output vector of force values f is constructed for training and validation. The measured force values are normalised to the interval $[0, 1]$ over the entire measurement data-set and denoted by $\overline{f} \in \mathbb{R}^{1\times n}$.

$$\overline{f} = \begin{bmatrix} f_1 & f_2 & \ldots & f_{n-1} & f_n \end{bmatrix} \tag{4}$$

For supervised learning of the NN, the data-set X_{ToF} was partitioned into training, validation, and test subsets containing 80%, 10%, and 10% of randomly selected data samples, respectively. In the final evaluation, model performance was assessed exclusively on the independent test set to ensure generalisation to previously unseen force magnitudes and experimental conditions.

The NN model evaluation method, characterising prediction accuracy, is based on the calculation of the mean absolute error (MAE) between the predicted force value $\hat{f}_i$ and the corresponding actual force f_i, defined as

$$\mathrm{MAE} = \frac{1}{n}\sum_{i=1}^{n} |\hat{f}_i - f_i|, \tag{5}$$

where n describes the number of measurement samples.

B. Neural-Network models

To achieve optimal performance in contact force prediction, three different NN model architectures were designed, implemented, and evaluated.

Single-input MLP: First, a single-input multilayer perceptron (MLP) comprising two hidden layers with 64 and 32 neurons, respectively, is evaluated. The NN model configuration is presented in Figure 11. Each hidden layer is followed by a

This article has been accepted for publication in IEEE Sensors Journal. This is the author's version which has not been fully edited and
content may change prior to final publication. Citation information: DOI 10.1109/JSEN.2026.3713612

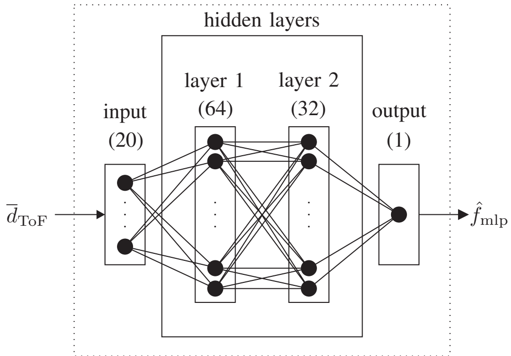

Fig. 11: The single-input MLP model comprises two hidden layers of 64 and 32 neurons, respectively. Each hidden layer is followed by a rectified linear unit (ReLU) activation function, and a dropout rate of $p = 0.3$ is applied after the first hidden layer. The vectorised ToF response $\overline{d}_{\mathrm{ToF}}$ serves as the input, and the model outputs a scalar normalised force prediction $\hat{f}_{\mathrm{mlp}}$.

rectified linear unit (ReLU) activation function, with a dropout rate of $p = 0.3$ applied after the first layer to mitigate overfitting.

Using $\overline{d}_{\mathrm{ToF}}$ as the single vectorised and normalised ToF response input, the output layer consists of one neuron producing a scalar of normalised force prediction $\hat{f}_{\mathrm{mlp}}$. Training is performed for 300 epochs.

Dual-input MLP: SoftSkin detects touch as a change in the histogram response, defined as a deviation from the baseline response illustrated in Figure 6. This simple touch-detection approach is valid under constant ambient-light conditions; however, the baseline is not static and may vary over time due to fluctuations in ambient illumination. Variations in ambient-light conditions manifest as a vertical shift in the histogram response.

To incorporate information about temporal ambient-light conditions, the NN configuration was extended to include a second input representing the temporal baseline. The resulting architecture, a dual-input MLP, is illustrated in Figure 12.

The baseline data-set was acquired independently prior to the ToF touch-detection measurements. Using the same preprocessing procedure as for the ToF data, the baseline data were organised into the array $B_{\mathrm{ToF}} \in \mathbb{R}^{20 \times n_B}$, where n_{B} denotes the number of baseline samples. Since $n_{\mathrm{B}} \ll n$, the mean baseline response b_{ToF} was computed over the time domain and subsequently normalised using the same linear transformation applied to d_{ToF}, yielding $\overline{b}_{\mathrm{ToF}}$.

The dual-input MLP comprises two inputs: the ToF response data $\overline{d}_{\mathrm{ToF}}$ and the temporal baseline response $\overline{b}_{\mathrm{ToF}}$. Each input is processed independently through a dedicated hidden layer with 32 neurons, followed by a ReLU activation function. The resulting feature representations are concatenated and passed to a shared second hidden layer with 32 neurons. After this layer, a ReLU activation is applied, followed by a dropout rate of $p = 0.3$. The final output layer produces a normalised scalar force prediction $\hat{f}_{\mathrm{mlp}}$.

Derivative-enhanced dual-input MLP: The first two NN models can be considered as static, as they do not incorporate

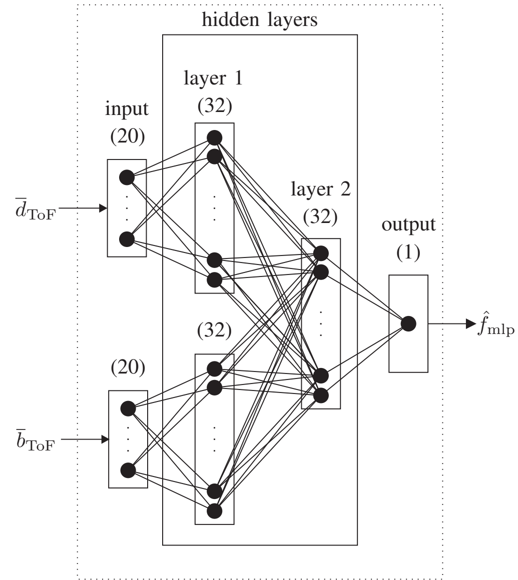

Fig. 12: The dual-input MLP model comprises two inputs: a vectorised ToF response $\overline{d}_{\mathrm{ToF}}$ and a temporal baseline response $\overline{b}_{\mathrm{ToF}}$. Each input is processed by an independent hidden layer with 32 neurons, followed by rectified linear unit (ReLu) activation function. The resulting features are then passed to a shared second hidden layer with 32 neurons, after which a ReLU activation and a dropout rate of $p = 0.3$ are applied. The output layer produces a scalar force prediction $\hat{f}_{\mathrm{mlp}}$.

information about the temporal dynamics of ToF sensor response changes. To investigate whether temporal dynamics could enhance model performance, the dual-input MLP was extended by incorporating first-order temporal derivatives of the photon-count signal into its inputs. The photon-response derivative d'_{ToF} at time t was computed using a second-order backward finite-difference method, defined as

$$d'_{\mathrm{ToF}}(t) = \frac{3d_{\mathrm{ToF}}(t) - 4d_{\mathrm{ToF}}(t - \Delta T) + d_{\mathrm{ToF}}(t - 2\Delta T)}{2\Delta T}, \tag{6}$$

where the vectorised $d_{\mathrm{ToF}}(t)$ denotes the ToF photon response at time t, and ΔT represents the sampling interval.

The derivative-enhanced dual-input MLP represents an extension of the dual-input MLP model. The photon-count response is augmented with its first temporal derivative, resulting in a combined input vector of 40 values, comprising 20 elements of the photon response $\overline{d}_{\mathrm{ToF}}$ and 20 elements of its temporal derivative d'_{ToF}. Accordingly, the first hidden layer associated with this input is expanded to 64 neurons. The configuration of the derivative-enhanced dual-input NN is illustrated in Figure 13.

The baseline branch remains unchanged relative to the dual-input MLP architecture.

Both branches are subsequently concatenated and passed through a shared output pathway comprising a second hidden layer with 32 neurons, followed by a ReLU activation and a dropout rate of $p = 0.3$. The output is a single scalar value representing the estimated force $\hat{f}_{\mathrm{mlp}}$.

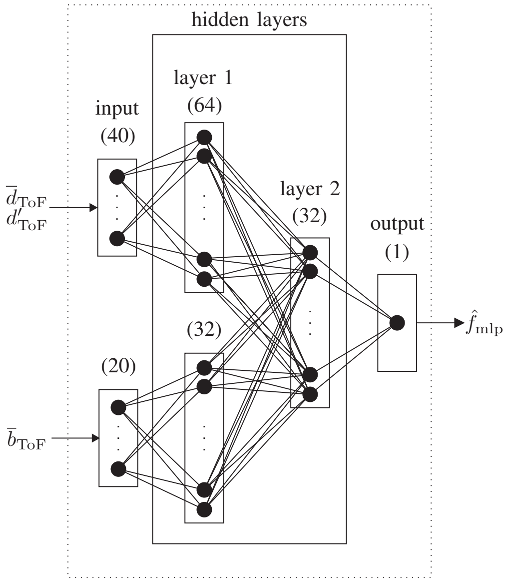

Fig. 13: The derivative-enhanced dual-input MLP model comprises two inputs: a concatenated vectorised ToF response $\bar{d}_{\mathrm{ToF}}$ with its temporal derivative d'_{ToF}, and a temporal baseline response $\bar{b}_{\mathrm{ToF}}$. Each input is processed by an independent hidden layer with 64 and 32 neurons, respectively, followed by a rectified linear unit (ReLU) activation function. The resulting features are then passed to a shared second hidden layer with 32 neurons, after which a ReLU activation and a dropout rate of $p = 0.3$ are applied. The output layer produces a scalar normalised force prediction $\hat{f}_{\mathrm{mlp}}$.

Random Forrest: To further improve prediction accuracy, a Random Forest (RF) regression model was introduced as a second-stage component following the MLP models. The RF estimates the residual error between the MLP prediction and the corresponding measured force. While the MLP captures the overall structure of the force signal, its predictions may underestimate or overshoot peak values, particularly at higher force levels. To compensate for these prediction errors, the RF was trained on the residuals of the training set using the same input features as the MLP. The RF model comprises 100 decision trees, each trained on a bootstrap sample of the training data, i.e., random subsets generated by sampling with replacement. The final scalar force prediction $\hat{f}$ is obtained as the sum of the MLP output $\hat{f}_{\mathrm{mlp}}$ and the RF residual estimate $\hat{f}_{\mathrm{rf}}$.

$$\hat{f} = \hat{f}_{\mathrm{mlp}} + \hat{f}_{\mathrm{rf}} \tag{7}$$

The final parallel MLP and RF architectures are illustrated in Figure 14.

Alternative NN models: The performance of the proposed three MLP NN models was additionally compared with four relatively simple alternative models: nonlinear regression, support vector regression (SVR), deep MLP, and gradient boosting (GB).

A nonlinear regression can capture simple nonlinear relationships while remaining relatively interpretable [21]. SVR estimates the output using only selected training samples (called support vectors) and can model nonlinear relationships via kernels. However, its performance and computational cost depend strongly on the kernel parameters and the number of support vectors [22]. A deep MLP uses multiple fully connected hidden layers with nonlinear functions to learn complex input-to-output mappings directly from data in an end-to-end manner [23]. GB builds an ensemble of weak regression trees sequentially, where each new tree corrects the remaining prediction error of the previous tree [24].

IV. Results

This section presents the performance evaluation of the proposed NN models for predicting applied force from ToF sensor response data. The primary performance metric is the mean absolute error (MAE), which compares the predicted force $\hat{f}_i$ with the corresponding actual force f_i, measured during physical interaction.

The resulting force predictions are visualised in Figures 15–19, each accompanied by a corresponding absolute error plot shown below. The numerical values of the calculated MAE for all three models are summarised in Table I.

Figure 15 presents the applied-force prediction for the single-input MLP-only model (see Figure 15a) and for the single-input MLP model with the RF parallel branch (see Figure 15b). The actual force measured by the force/torque sensor is shown in blue, while the NN model prediction is shown in orange. Detailed sections in Figure 15 further illustrate the zoomed-in correspondence between the predicted and the measured force signals. The magnitude of the applied force is displayed on the vertical axis, and time is shown on the horizontal axis.

A more detailed view of the force predictions and the corresponding applied force values at different indentation velocities is presented in Figure 16 for the single-input MLP, in Figure 17 for the dual-input MLP, and in Figure 18 for the derivative-enhanced dual-input MLP. Predicted force values are shown in red, the measured applied force in blue, and the prediction error in magenta in a separate subplot. The left, middle, and right plots correspond to indentation velocities of $v_1 = 0.1$ mm/s, $v_2 = 1.0$ mm/s, and $v_3 = 5.0$ mm/s, respectively. Despite the different indentation velocities, the duration of maintaining the contact at the target position was identical in all cases, i.e., $T_{\mathrm{touch}} = 5$ s.

Figure 19 presents a combined view of the force-prediction performance for all three parallel NN models. Red curves

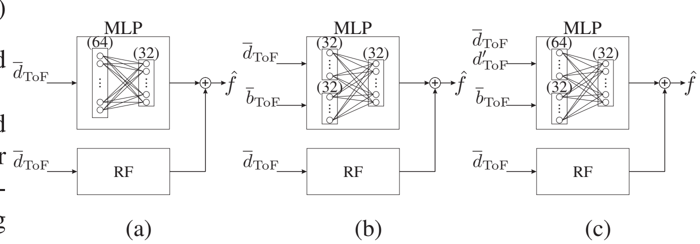

Fig. 14: Three different MLP model architectures with a parallel RF regression model: (a) single-input MLP, (b) dual-input MLP, and (c) derivative-enhanced dual-input MLP.

This article has been accepted for publication in IEEE Sensors Journal. This is the author's version which has not been fully edited and
content may change prior to final publication. Citation information: DOI 10.1109/JSEN.2026.3713612

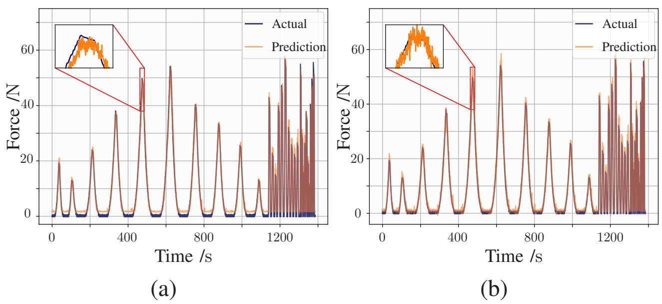

Fig. 15: Actual applied force and force prediction for Single-input MLP: (a) MLP only output with MAE 1.35 N, and (b) MLP-RF output with MAE 0.94 N.

denote predictions obtained using the single-input method, blue curves correspond to the dual-input model, and green curves represent the derivative-enhanced dual-input model. In contrast, black curves indicate the actual force value. The left, middle, and right plots correspond to a single peak (touch) of applied pressure at indentation velocities of $v_1 = 0.1$ mm/s, $v_2 = 1.0$ mm/s, and $v_3 = 5.0$ mm/s, respectively. The applied force at these peaks is approximately 15 N, a value not included in the training data-set. For improved visual clarity, the NN prediction outputs are filtered using a 5th-order Butterworth filter with a cutoff frequency of 10 Hz.

Table I summarises the calculated MAE values, expressed in N, for all three NN models and the estimated number of arithmetic calculations per single prediction. Each row corresponds to an individual NN model, while the columns represent subsets associated with specific indentation velocities. The second-to-last column reports the overall MAE across the entire measurement set for each model. The last column represents the calculation cost for a single prediction. The upper segment of the table presents results for the MLP-only models, whereas the second segment shows results obtained from the parallel MLP–RF configurations. In subsequent segments, results from other simpler/alternative models are presented: nonlinear regression, support vector regression (SVR), a deep MLP, and a GB method.

V. Discussion

The primary objective of this work was to investigate whether the applied force can be estimated from the optical response of the ToF sensor within SoftSkin. The analysis was limited to contacts at a single point. In addition to achieving accurate steady-state force estimates, the study demonstrated that dynamic tracking of the contact force is possible.

Observation of Figures 15–19 confirms the feasibility of predicting the applied force directly from optical measurements using nonlinear modelling. An indenter applying force deforms SoftSkin and generates an optical response within the contact region. Across all three NN models shown in Figures 16–18, the predicted force values (red) closely follow the measured reference values (blue) in general terms. When comparing the individual NN models, it should be noted that the indentation duration for velocity v_1 is substantially longer than for the other two cases (v_2 and v_3). However, the stationary contact time at the applied force, $T_{\text{touch}} = 5$ s, is identical for all cases.

First, we compare the standalone MLP model with the model incorporating an RF residual corrector, as shown in Figure 15. This comparison demonstrates that residual learning systematically improves applied-force estimation. While the MLP captures the overall signal dynamics, its predictions exhibit systematic deviations at the extremes of the force range. Low forces tend to be overestimated, whereas peak forces are consistently underestimated, indicating a limited ability of the MLP to generalise beyond the mid-range values that dominate the training distribution (Figure 15a). From an engineering perspective, the MLP component can be viewed as analogous to the proportional term in a process controller, for which steady-state error cannot be eliminated. Consequently, the predicted force cannot perfectly match the nominal force value.

By modelling the residual errors between the MLP predictions and the actual force values, the RF stage reduces high-frequency fluctuations and corrects systematic bias, resulting in predictions that are both smoother and more closely aligned with the ground truth (Figure 15b). The reduced prediction error highlights the complementary nature of the hybrid design: the MLP provides a global approximation of the force dynamics, whereas the RF effectively compensates for localised nonlinearities and residual error, thereby improving robustness across varying input conditions.

The data collected in Table I, containing calculated MAE values, further confirms the satisfactory accuracy of the force prediction. Overall mean values of absolute errors between the prediction and the actual value are less than 1.55 N in all cases. The smallest MAE is observed at the penetration velocity v_1, whereas the largest occurs at velocity v_3. Moreover, incorporating parallel RF regression reduces the MAE by more than 30 %, and the MAE of the parallel MLP-RF model at v_3 is lower than that of the MLP-only model at v_2.

The differences among the predictions of the single-input, dual-input, and derivative-enhanced dual-input models are less pronounced than those observed between the MLP-only and MLP–RF configurations. The largest differences in MAE occur for the MLP-only models at v_1, whereas in the remaining cases the differences are below 0.2 N. The MAE values computed over the entire test set (last column in Table I) differ by only 0.06 N, which is practically negligible. The single-input model exhibits the highest error, whereas the derivative-enhanced dual-input model achieves the lowest error.

Inspection of Figures 16–18, which individually present the prediction responses of the three NN models, highlights the importance of analysing the error between the predicted and measured force values (shown in magenta). The first observation is that the prediction error increases with higher applied forces. This trend is most pronounced at the lowest indentation velocity ($v_1 = 0.1$ mm/s), although the error rarely exceeds 5 N. A closer examination of Figures 16a, 17a, and 18a, corresponding to force predictions at indentation velocity v_1, reveals slightly noisier behaviour for the single-input method. Additional error spikes are observed for the

This article has been accepted for publication in IEEE Sensors Journal. This is the author's version which has not been fully edited and content may change prior to final publication. Citation information: DOI 10.1109/JSEN.2026.3713612

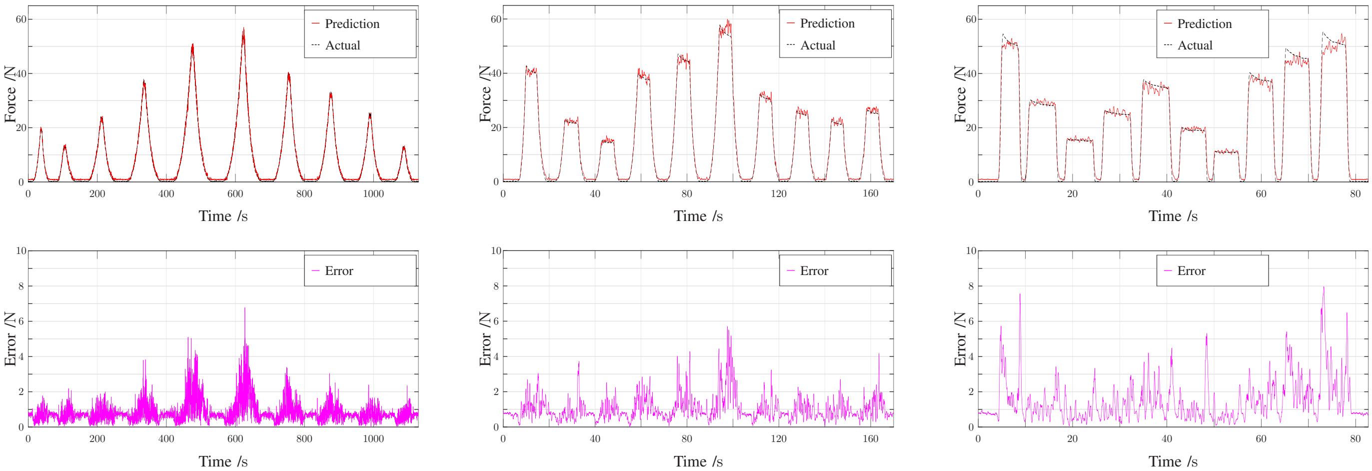

(a) (b) (c)

Fig. 16: Actual applied force and predicted force for the single-input model at indentation velocities: (a) $v_1 = 0.1$ mm/s, (b) $v_2 = 1.0$ mm/s, and (c) $v_3 = 5.0$ mm/s.

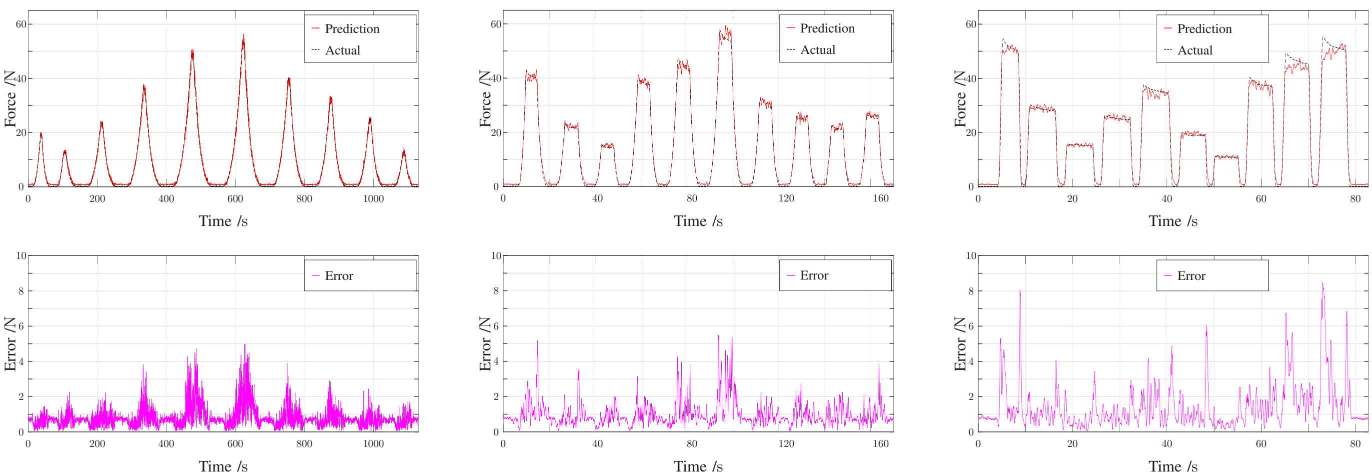

(a) (b) (c)

Fig. 17: Actual applied force and predicted force for a dual-input model at indentation velocities: (a) $v_1 = 0.1$ mm/s, (b) $v_2 = 1.0$ mm/s, and (c) $v_3 = 5.0$ mm/s.

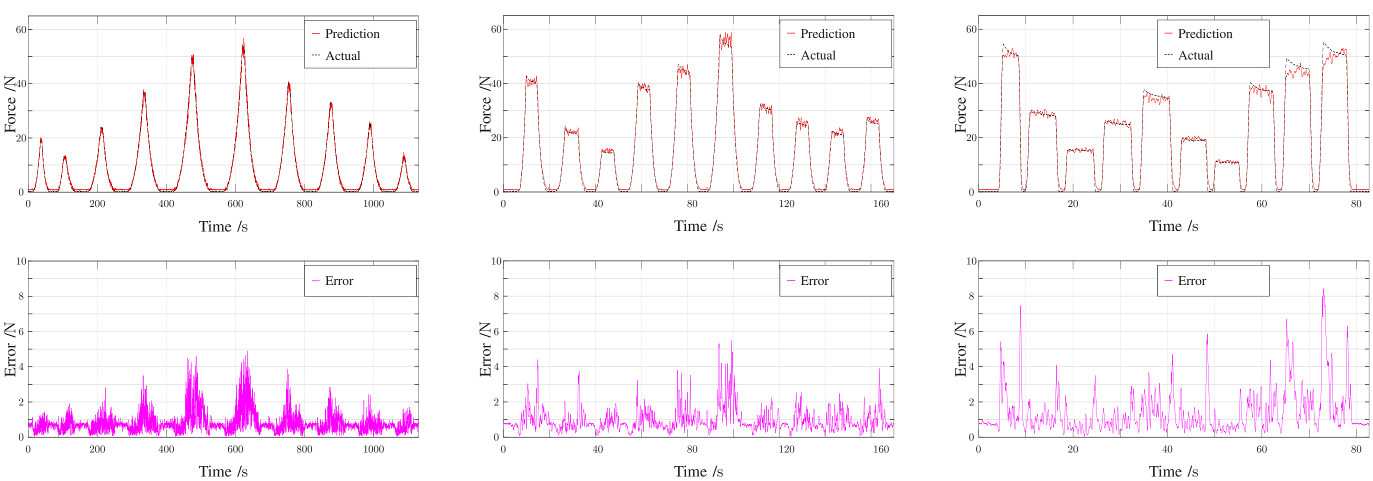

(a) (b) (c)

Fig. 18: Actual applied force and predicted force for a derivative-enhanced dual-input model at indentation velocities: (a) $v_1 = 0.1$ mm/s, (b) $v_2 = 1.0$ mm/s, and (c) $v_3 = 5.0$ mm/s.

This article has been accepted for publication in IEEE Sensors Journal. This is the author's version which has not been fully edited and
content may change prior to final publication. Citation information: DOI 10.1109/JSEN.2026.3713612

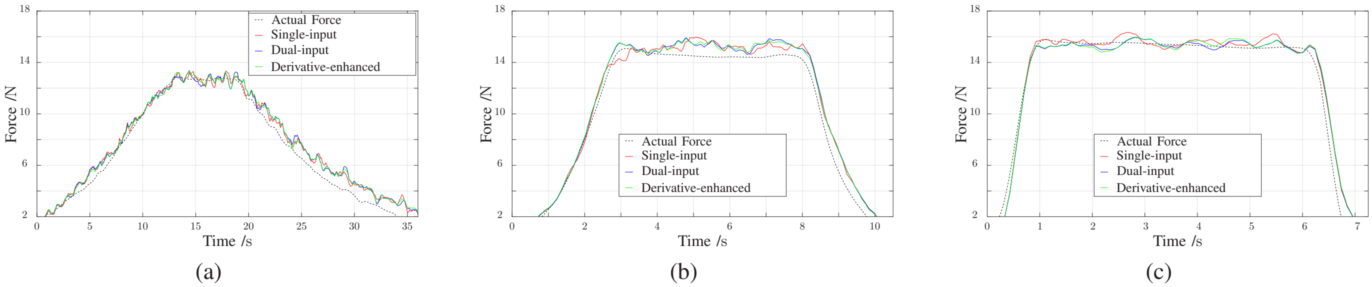

Fig. 19: Zoomed view of force-prediction results for the single-input MLP (red), dual-input MLP (blue), and derivative-enhanced dual-input MLP (green), together with the actual force value (black), for a single applied touch at indentation velocities: (a) $v_1 = 0.1$ mm/s, (b) $v_2 = 1.0$ mm/s, and (c) $v_3 = 5.0$ mm/s.

TABLE I: Mean absolute error (MAE) results for all three MLP models without RF regression and with parallel RF regression at different indentation velocities.

	Mean absolute error - MAE /N				
NN method	$v_1 = 0.1$ mm/s	$v_2 = 1.0$ mm/s	$v_3 = 5.0$ mm/s	Overall	Calculation cost per prediction
MLP only:					
Single-input	1.2651	1.4617	2.1393	1.3469	
Dual-input	1.4521	1.7090	2.1993	1.5334	≈ 6.7k operations
Derivative-enhanced	1.0912	1.5011	2.0342	1.2037	
MLP and RF:					
Single-input	0.8134	1.0431	1.4848	0.9373	
Dual-input	0.7888	1.0030	1.4344	0.8856	≈ 8.7k operations
Derivative-enhanced	0.7862	0.9885	1.4491	0.8759	
Nonlinear regression:					
Single-input	1.0034	1.2236	1.6505	1.0692	
Dual-input	0.9486	1.2148	1.6386	1.0226	≈ 2.5k operations
Derivative-enhanced	0.9474	1.2140	1.6388	1.0216	
Support vector regression:					
Single-input	0.9577	1.4605	1.8553	1.0732	
Dual-input	0.9734	1.5622	1.9416	1.1037	≈ 12.2M operations
Derivative-enhanced	1.1494	1.8941	2.4805	1.3206	
Deep MLP:					
Single-input	1.1973	1.3688	1.7040	1.2487	
Dual-input	1.2737	1.6580	2.0307	1.3662	≈ 50.2k operations
Derivative-enhanced	1.3686	1.5777	2.0592	1.4356	
Gradient boosting:					
Single-input	0.8350	1.0863	1.5140	0.9065	
Dual-input	0.8461	1.1952	1.5978	0.9340	≈ 1.2k operations
Derivative-enhanced	0.8472	1.1937	1.5978	0.9347	

single-input model, whereas the error curves are considerably smoother for both dual-input models. At higher indentation velocities (v_2 and v_3), the force prediction appears noisier than for v_1; however, this is primarily due to the reduced number of time samples. While the stationary contact time T_{touch} remains constant, the indentation duration is proportionally shorter (by factors of approximately 10 and 50, respectively).

Focusing on Figures 16c, 17c, and 18c, the largest deviations in the predicted force values occur during transitions between zero pressure and the target applied force (and vice versa). When the applied force is held constant, the error between the predicted and measured force values is significantly smaller. Table I indicates that the maximum average error occurs at the steady-state condition of penetration with the highest robot velocity, v_3. In this regime, transient effects are most pronounced due to the ToF sensor's limited sampling frequency (9 Hz). During force increase and release, the sensor response is too slow to capture sufficient measurements for a smooth transition and accurate subsequent prediction (leading to high spikes at force transitions). It is also important to note that at the maximum robot velocity, the duration of measurements with near-zero applied force is substantially shorter, resulting in smaller minimum prediction errors than in the cases of v_1 and v_2.

The maximum contact force prediction variability in stationary contacts is at v_2 indentation velocity at ≈ 55 N of applied force and equals 1.94 N, but normally < 1.5 N. From the Error graphs in Figures 16-18, higher variability is also observed with increased applied force. The mean absolute error between the force prediction $\hat{f}_i$ and the actual force f_i at stationary contacts equals 0.65 N.

Figure 19 presents zoomed-in views of the predicted and measured applied-force signals for all three indentation velocities. As noted earlier, the responses of the individual prediction methods do not differ substantially across different force-application rates. The primary differences are observed in the noise level and in the decay rate of transient effects.

Comparing the predictions of the other simple/alternative NN models in Table I, the nonlinear regression, SVR, and gradient boosting methods have similar overall MAE values. For all listed methods, performance is close to that of the MLP+RF method, but the MAE increases more pronouncedly with increasing penetration velocity. The worst performance is observed with a deep MLP model. The time spent on network training is also meaningful. Only the nonlinear regression had a shorter training time compared to the MLP+RF method ($\approx 2\ \mathrm{min}$). The other methods had a training time at least 2-5 times longer. It took the longest to learn for the SVR method ($\approx 2\ \mathrm{h}$).

Computational cost per prediction is one of the most important metrics for real-time deployment. GB has the fewest arithmetic calculations per prediction, with an MAE similar to that of the MLP+RF model, which has approximately 7 times higher computational cost. Nonlinear regression requires twice as many operations per prediction as GB. The highest number of calculations is required for SVR, 10000 times that of GB.

The presented SoftSkin results show promising overall performance compared to other optical touch-sensing approaches [6], [7]. The spatial resolution is much lower than in camera-based visuotactile sensors [6], but SoftSkin offers strong spatial scalability. Besides its primary role in touch localisation, the force prediction error of $< 1\ \mathrm{N}$ over the range up to $50\ \mathrm{N}$ is promising.

The current work is a proof-of-concept study on force prediction using optical ToF responses. By incorporating exponential decay of the peak signal intensity with distance from the ToF sensor [25] into a prediction model, a spatial generalisation of force prediction can be achieved. As the distance from the ToF sensor increases (shifting the middle peak in the histogram to higher bin values), the number of detected photons decreases, thereby reducing the resolution. An alternative approach to spatial generalisation would be to extend the training data-set to the entire SoftSkin sensing area. This option would require a significant increase in data acquisition and model training effort.

VI. Conclusion

The use of ToF sensors embedded in optically transparent materials enables effective sensorization of large areas without the need for wiring individual taxels, and this approach has already proven successful for tactile location detection. This work further investigates the potential of employing the same principle to predict contact forces from ToF sensor data using machine-learning methods, thereby extending the functionality of the SoftSkin sensor. A robotic experimental setup was used to acquire datasets across multiple indentation velocities and force levels, ensuring variability and independence between the training and test sets. To model the nonlinear relationship between sensor readings and applied forces, three multilayer perceptron (MLP) architectures were developed and analysed: a single-input model, a dual-input model incorporating baseline information, and a derivative-enhanced dual-input model. To further improve prediction accuracy, a two-stage architecture was introduced in which a Random Forest (RF) regressor was trained on the residuals of the MLP predictions.

The results demonstrate that standalone MLP models capture the general force profile but do not achieve satisfactory prediction accuracy. Their errors remain relatively high and inconsistent across preprocessing settings, with systematic deviations particularly evident at low and high force levels. Introducing the RF residual corrector substantially reduces these deviations, resulting in smoother predictions and lower mean absolute errors.

Overall mean absolute error in force prediction for all three algorithms was lower than $1.55\ \mathrm{N}$. The lowest error in applied force prediction was, as expected, at the lowest indentation velocity of $0.1\ \mathrm{mm/s}$ and using the derivative-enhanced dual-input method. Nevertheless, the numerical differences in MAE calculations are in the range of $0.06\ \mathrm{N}$. It is evident that, with an increase in indentation velocity, the calculated MAE also increases. More significant errors occur during sudden and significant changes in applied force. The combination of NNs with ensemble-based residual correction effectively balances global signal approximation with localised error compensation, resulting in improved robustness and accuracy.

The presented study serves as a proof-of-concept demonstrating the SoftSkin sensory surface's capability for contact-force sensing. The results confirm that tactile force estimation based on ToF signal acquisition within an optically transparent soft material, combined with machine-learning methods, is both viable and accurate. Although the study was conducted for a single location at the sensory surface, the findings can be generalised to the entire sensorised area by extending the neural network architecture. Despite current limitations to single-point force prediction, software for data acquisition and force estimation is ready for real-time deployment. Integrating force-measurement capability alongside tactile localisation opens new opportunities and potential applications for the ToF-based optical SoftSkin sensor in collaborative robotics and other fields that require feedback on tactile location and contact force. Transient effects are most pronounced due to the ToF sensor's limited sampling frequency ($9\ \mathrm{Hz}$). The incorporation of newer versions of ToF sensors already on the market, which provide higher sampling frame rates, would increase the capability to predict transient forces at higher indentation velocity.

Acknowledgment

During the preparation this work authors used OpenAI models solely to improve language quality and readability. After using this tool/service, the authors reviewed and edited the content as needed and take full responsibility for the content of the submitted article.

The authors would like to thank Professor Grega Bizjak from the Laboratory of Lighting and Photometry (University of Ljubljana, Faculty of Electrical Engineering) for providing us the equipment for illuminance measurement.

REFERENCES

[1] A. M. Almassri, W. Z. Wan Hasan, S. A. Ahmad, A. J. Ishak, A. M. Ghazali, D. N. Talib, and C. Wada, "Pressure sensor: State of the art, design, and application for robotic hand," *Journal of Sensors*, 2015. DOI: 10.1155/2015/846487.

[2] S. R. A. Ruth, V. R. Feig, H. Tran, and Z. Bao, "Microengineering pressure sensor active layers for improved performance," *Advanced Functional Materials*, vol. 30, no. 39, 2020. DOI: 10.1002/adfm.202003491.

[3] L. Guo, G. Wu, Q. Wang, T. Li, B. Yao, Y. Zou, and M. Xu, "Advances in triboelectric pressure sensors," *Sensors and Actuators A: Physical*, vol. 355, 2023. DOI: 10.1016/j.sna.2023.114331.

[4] P. Woolf, "Pressure sensors," in *Chemical Process Dynamics and Controls*, 4th ed. LibreTexts, University of Michigan, 2025, Open Education Resource (OER) textbook, accessed 23.09.2025. [Online]. Available: https://eng.libretexts.org/Bookshelves/Industrial_and_Systems_Engineering/Chemical_Process_Dynamics_and_Controls_(Woolf)/03%3A_Sensors_and_Actuators/3.03%3A_Pressure_Sensors.

[5] S. Kumari, "Optical pressure sensor: A review," *International Journal of Applied Engineering Research*, vol. 10, no. 1, pp. 17 891–17 908, 2015.

[6] M. Lambeta, P.-W. Chou, S. Tian, B. Yang, B. Maloon, V. R. Most, D. Stroud, R. Santos, A. Byagowi, G. Kammerer, D. Jayaraman, and R. Calandra, "Digit: A novel design for a low-cost compact high-resolution tactile sensor with application to in-hand manipulation," *IEEE Robotics and Automation Letters*, vol. 5, no. 3, pp. 3838–3845, 2020. DOI: 10.1109/LRA.2020.2977257.

[7] G. Lu, S. Fu, and Y. Xu, "Design and experimental research of robot finger sliding tactile sensor based on fbg," *Sensors*, vol. 22, no. 21, 2022, ISSN: 1424-8220. DOI: 10.3390/s22218390. [Online]. Available: https://www.mdpi.com/1424-8220/22/21/8390.

[8] S. S. Desai, A. M. Eckert-Erdheim, and A. M. Hoover, "A large-area tactile force sensor for measuring ground reaction forces from small legged robots," in *2013 IEEE/RSJ International Conference on Intelligent Robots and Systems*, 2013, pp. 4753–4758. DOI: 10.1109/IROS.2013.6697041.

[9] A. J. Fernandez, H. Weng, P. B. Umbanhowar, and K. M. Lynch, "Visiflex: A low-cost compliant tactile fingertip for force, torque, and contact sensing," *IEEE Robotics and Automation Letters*, vol. 6, no. 2, pp. 3009–3016, 2021. DOI: 10.1109/LRA.2021.3061378.

[10] R. Wattanaparinton and K. Takemura, "Vision-based tactile sensing using multiple contact images generated by re-propagated frustrated total internal reflections," in *2022 IEEE International Conference on Systems, Man, and Cybernetics (SMC)*, 2022, pp. 962–967. DOI: 10.1109/SMC53654.2022.9945094.

[11] J.-T. Lin, C. A. Newquist, and C. K. Harnett, "Multitouch pressure sensing with soft optical time-of-flight sensors," *IEEE Transactions on Instrumentation and Measurement*, vol. 71, pp. 1–8, 2022. DOI: 10.1109/TIM.2022.3141159.

[12] E. Bacher, S. Cartiel, J. García-Pueyo, J. Stopar, A. Zore, R. Kamnik, I. Aulika, A. Ogurcovs, J. Grūbe, A. Bundulis, J. Butikova, M. Kemere, A. Muñoz, and M. Laurenzis, "Optoskin: Novel lidar touch sensors for detection of touch and pressure within wave guides," *IEEE Sensors Journal*, vol. 24, no. 20, pp. 33 268–33 280, 2024. DOI: 10.1109/JSEN.2024.3443615.

[13] C. M. Bishop, "Neural networks and their applications," *Review of Scientific Instruments*, vol. 65, no. 6, pp. 1803–1832, 1994. DOI: 10.1063/1.1144830.

[14] T. Radhakrishnan and U. Nandan, "Milling force prediction using regression and neural networks," *Journal of Intelligent Manufacturing*, vol. 16, no. 1, pp. 93–102, 2005. DOI: 10.1007/s10845-005-4826-4.

[15] R. Jain, M. Lal Meena, M. Kumar Sain, and G. Sharan Dangayach, "Pulling force prediction using neural networks," *International Journal of Occupational Safety and Ergonomics (JOSE)*, vol. 25, no. 2, pp. 194–199, 2019. DOI: 10.1080/10803548.2018.1443899.

[16] V. Kakani, X. Cui, M. Ma, and H. Kim, "Vision-based tactile sensor mechanism for the estimation of contact position and force distribution using deep learning," *Sensors*, vol. 21, no. 5, 2021, ISSN: 1424-8220. DOI: 10.3390/s21051920.

[17] S. Min, H. Geng, Y. He, W. Liang, S. Chen, Z. Wang, Q. Liu, and T. Xu, "A stretchable tactile sensor with deep learning-enabled 3d force decoding for human and robotic interfaces," *Chemical Engineering Journal*, vol. 521, p. 167 189, 2025, ISSN: 1385-8947. DOI: https://doi.org/10.1016/j.cej.2025.167189.

[18] *Durometer shore hardness scale*, https://www.smooth-on.com/page/durometer-shore-hardness-scale/, Accessed: 2026-02-16.

[19] I. Aulika, A. Ogurcovs, M. Kemere, A. Bundulis, J. Butikova, K. Kundzins, E. Bacher, M. Laurenzis, S. Schertzer, J. Stopar, A. Zore, and R. Kamnik, "Influence of material optical properties in direct tof lidar optical tactile sensing: Comprehensive evaluation," *Materials*, vol. 18, no. 14, 2025, ISSN: 1996-1944. DOI: 10.3390/ma18143287. [Online]. Available: https://www.mdpi.com/1996-1944/18/14/3287.

[20] M. Born and E. Wolf, *Principles of optics: electromagnetic theory of propagation, interference and diffraction of light*. Elsevier, 2013.

[21] C. M. Bishop, *Pattern Recognition and Machine Learning*, ser. Information Science and Statistics. New York, NY: Springer, 2006, ISBN: 978-0-387-31073-2.

[22] A. J. Smola and B. Schölkopf, "A tutorial on support vector regression," *Statistics and Computing*, vol. 14,

no. 3, pp. 199–222, 2004. DOI: 10.1023/B:STCO.0000035301.49549.88.

[23] G. Cybenko, "Approximation by superpositions of a sigmoidal function," *Mathematics of Control, Signals and Systems*, vol. 2, no. 4, pp. 303–314, 1989. DOI: 10.1007/BF02551274.

[24] J. H. Friedman, "Greedy function approximation: A gradient boosting machine," *The Annals of Statistics*, vol. 29, no. 5, pp. 1189–1232, 2001. DOI: 10.1214/aos/1013203451.

[25] A. Ogurcovs, I. Aulika, S. Cartiel, M. Kemere, J. Butikova, and E. Sledevskis, "Advancing multi-touch sensing: Integrating ftir and tof technologies for precise and large-scale touch interfaces," *Sensors*, vol. 25, no. 17, 2025, ISSN: 1424-8220. DOI: 10.3390/s25175503. [Online]. Available: https://www.mdpi.com/1424-8220/25/17/5503.

Aleš Zore received the Ph.D. degree in electrical engineering from the University of Ljubljana, Slovenia, in 2024. He is currently a researcher in Laboratory of Robotics at Faculty of Electrical Engineering at University of Ljubljana. His latest research focuses are development of adaptive robotic cell and development of SoftSkin for human-robot enhanced safety.

Marina Babić received the master's degree in electrical engineering from the University of Ljubljana, Ljubljana, Slovenia, in 2025. She is currently employed as a Researcher with the Laboratory of Robotics, University of Ljubljana. Her research interests lie primarily in the field of artificial intelligence, robotics, and biomedical technology.

Marko Munih received the Ph.D. degree in electrical engineering from the Faculty of Electrical Engineering, University of Ljubljana (UL), Ljubljana, Slovenia. From 2004 to 2006, he was the Head of the Department for Measurements and Process Control, Faculty of Electrical Engineering, UL, where he is currently a Full Professor and the Head of the Laboratory of Robotics. In the last 15 years is his interest focused on robot contact with environment, as well as construction and use of haptic interfaces in the fields of industry and rehabilitation engineering, in combination with VR. Notable impact had research on physiological computing linked to rehabilitation robotics.

Roman Kamnik received the D.Sc degree in electrical engineering from University of Ljubljana, Faculty of Electrical Engineering, Ljubljana, Slovenia, in 1999. He is currently a senior researcher in the Laboratory of Robotics and Full Professor at Faculty of Electrical Engineering, University of Ljubljana. His research interests are focused to the biomedical engineering and robotics. He is specialized in the development of intelligent robotic devices with the applications in sport, industrial and rehabilitation robotics, and transport.